High frame rate multi-perspective cardiac ultrasound imaging using phased array probes

Ultrasonics 123 (2022) 106701

Contents lists available at ScienceDirect

Ultrasonics

journal homepage: www.elsevier.com/locate/ultras

High frame rate multi-perspective cardiac ultrasound imaging using phased array probes

Peilu Liu *, Hein de Hoop, Hans-Martin Schwab, Richard G.P. Lopata

Photoacoustics & Ultrasound Laboratory Eindhoven (PULS/e), Department of Biomedical Engineering, Eindhoven University of Technology, Eindhoven, Netherlands

ARTICLE INFO

Keywords:
Ultrasound
Multi-perspective
High frame rate
Echocardiography
Image enhancement
Image registration
Image fusion
Speckle statistics

ABSTRACT

Ultrasound (US) imaging is used to assess cardiac disease by assessing the geometry and function of the heart utilizing its high spatial and temporal resolution. However, because of physical constraints, drawbacks of US include limited field-of-view, refraction, resolution and contrast anisotropy. These issues cannot be resolved when using a single probe. Here, an interleaved multi-perspective 2-D US imaging system was introduced, aiming at improved imaging of the left ventricle (LV) of the heart by acquiring US data from two separate phased array probes simultaneously at a high frame rate.

In an *ex-vivo* experiment of a beating porcine heart, parasternal long-axis and apical views of the left ventricle were acquired using two phased array probes. Interleaved multi-probe US data were acquired at a frame rate of 170 frames per second (FPS) using diverging wave imaging under 11 angles. Image registration and fusion algorithms were developed to align and fuse the US images from two different probes. First- and second-order speckle statistics were computed to characterize the resulting probability distribution function and point spread function of the multi-probe image data.

First-order speckle analysis showed less overlap of the histograms (reduction of 34.4%) and higher contrast-to-noise ratio (CNR, increase of 27.3%) between endocardium and myocardium in the fused images. Autocorrelation results showed an improved and more isotropic resolution for the multi-perspective images (single-perspective: 0.59 mm × 0.21 mm, multi-perspective: 0.35 mm × 0.18 mm). Moreover, mean gradient (MG) (increase of 74.4%) and entropy (increase of 23.1%) results indicated that image details of the myocardial tissue can be better observed after fusion.

To conclude, interleaved multi-perspective high frame rate US imaging was developed and demonstrated in an *ex-vivo* experimental setup, revealing enlarged field-of-view, and improved image contrast and resolution of cardiac images.

1. Introduction

Echocardiography is a widely used imaging tool that is commonly used for diagnosis and monitoring of cardiac disease providing comprehensive cardiac images to assess cardiac geometry and detect geometric abnormalities non-invasively [1]. Major advantages compared to other image modalities are its ease of use, low cost, portability, and the ability to perform functional imaging, such as Doppler or vector flow measurements, strain imaging, and elastography. Combined with the high spatial and temporal resolution, US is the modality of choice for imaging and functional measurements of the cardiovascular system to detect cardiac diseases.

US, however, does have several shortcomings because of physical constraints. Compared to computed tomography (CT) and magnetic resonance imaging (MRI), the field-of-view is limited. In cardiac imaging, a large field-of-view is needed to visualize e.g. left ventricular function, let alone all four chambers. In addition, US images have a granular appearance, so-called speckle, caused by interference of the waves. Because of speckle, refraction, diffraction, and absorption of acoustic energy, the tissue contrast in echocardiographic images can be low [2]. Moreover, appearance of edges depends on the direction of the sound propagation and the signal-to-noise (SNR) and resolution decrease with increasing imaging depth [3], which will eventually reduce the accuracy of derived measurements, such as wall and cavity volume, or wall motion and deformation.

Conventional line-by-line and focused US can achieve relatively high

* Corresponding author.
E-mail address: p.liu4@tue.nl (P. Liu).

https://doi.org/10.1016/j.ultras.2022.106701
Received 19 May 2021; Received in revised form 14 December 2021; Accepted 2 February 2022
Available online 5 February 2022

resolution and SNR as a cost of low frame rate [4,5]. The heart, however, is a dynamic and complex organ. Moving structures (e.g. heart valves) are not easily imaged and diagnosis may be impaired by a relatively low frame rate or spatial resolution. In recent years, ultrafast US imaging is replacing conventional focused US, thereby overcoming the original frame rate limitations, leading to improved motion tracking and accurate quantification and visualization of contraction patterns in the heart [6,7]. But image quality, e.g., resolution and contrast, is inherently worse than in conventional US imaging. To solve this issue, spatial coherent compounding was introduced, which can improve lateral resolution and overall SNR to levels comparable to focused US imaging techniques [8,9]. Unfortunately, spatial coherent compounding is only effective in a small overlapping region-of-interest for deeper lying structures [10]. Moreover, due to the presence and anatomy of the ribs, a relatively small aperture size can be used (i.e., phased array transducer) as well as a limited number of steering angles, reducing the effective region-of-interest even further.

CT and MRI are commonly treated as the gold standard for geometry assessment of the heart, due to excellent contrast and wide field-of-view [11,12]. However, these alternatives are costly and often require contrast agents. Additionally, CT imposes a higher burden on patients because of the exposure to ionizing radiation [13]. MRI suffers from a low temporal resolution in 3-D, hence it is difficult to perform strain imaging and estimate material parameters of the cardiac wall. Other disadvantages of MRI consist of long scanning time and poor suitableness due to implants [14].

Multi-view US imaging has been introduced to improve image quality for cardiac application [15,16]. LV image quality was improved by fusing multiple 3-D volumes acquired at different positions and points in time [17,18]. In a comparable study, wide view transesophageal echocardiography was used to enhance the accuracy of segmentation of heart cavities [19]. A registration method was developed to align and fuse images acquired from different imaging windows [20]. All these methods have shown positive results, leading to a larger field-of-view and improved image contrast. The major shortcoming, however, is the fact that images were acquired manually, at relatively low volume rates and at different time points, which will result in decorrelation of the images, and therefore lower the accuracy of the image enhancement (e.g., post registration and fusion). Considering the large motion and contraction of the heart, and variability in heart rate from cycle to cycle, a different approach based on multi-perspective US imaging that can perform high frame rate, interleaved imaging would greatly enhance performance.

Interleaved multi-perspective imaging has been proposed in [21,22], showing promising improvements in image quality in phantoms. In parallel, an interleaved multi-perspective US imaging method was developed for aortic imaging. Improvements in image quality and vascular strain imaging were demonstrated in a mock circulation setup using a porcine aorta [23]. Advantages of interleaved multi-perspective imaging have been shown in the aforementioned studies, but was based on curved and linear arrays under conditions where no to little motion was present. However, for cardiac imaging, a dedicated system based on phased array transducers with a high frame rate is required, tested under realistic (*ex-vivo* beating hearts) conditions, to demonstrate and validate this approach before translation into the clinic.

In this study, a high frame rate interleaved multi-perspective US imaging system was introduced based on two phased array probes for cardiac imaging. The performance was tested experimentally using a sophisticated beating porcine heart setup [24]. A semi-automatic image registration and two image fusion algorithms were developed to register and fuse the US images obtained from the two different probes. Image gradient and entropy were calculated to evaluate the performances of the two fusion algorithms. First- and second-order speckle statistics were computed to analyze the improvements in image resolution and contrast between endocardium and myocardium.

2. Methods

2.1. Experimental setup and data acquisition

A total of three hearts were explanted from landrace hybrid pigs, slaughtered for human consumption at the slaughterhouse. All three hearts were isolated and perfused with cold cardioplegic solution after exsanguination. After 2 mins warm ischemic time, all the hearts were transported to the laboratory (LifeTec Group, Eindhoven, NL) instantly after exsanguination for the upcoming experiments. The protocols of the slaughterhouse and laboratory were in accordance with EC regulations 1069/2009 regarding the use of slaughterhouse animal material for diagnosis and research, supervised by the Dutch Government (Dutch Ministry of Agriculture, Nature and Food Quality) and approved by the associated legal authorities of animal welfare (Food and Consumer Product Safety Authority).

In the *ex-vivo* experimental setup, the hearts were paced at a rate between 90 and 120 beats per min (bmp) to assure a steady heart rhythm through the whole experiment. The hearts were entirely submerged in a saline solution at 38 °C in order to perform US imaging. More details about the setup of the beating porcine hearts can be found in [24].

US Data were acquired using a 256-channel Vantage open research system (Verasonics, Redmond, USA) equipped with two phased array probes (type: P4-2v, center frequency: 2.95 MHz, bandwidth: 1.64–4.26 MHz).

Parasternal long-axis (PS) and apical (AP) views of the LV were acquired with two phased array probes, as shown in Fig. 1. The two probes were attached to a mini-arch to ensure that they were exactly imaging the same axial – lateral plane with a relative angle of 90°. To avoid interference, the two separate probes were acquiring US data with an interleaved scanning sequence, where each probe took turns to transmit and receive US signals. Each probe transmitted and received 11 steered diverging waves between −12° and 12° (with respect to the origin of each probe) to perform coherent diverging wave compounding, where image contrast would benefit the most by increasing the number of steering angles [6]. Continually increasing the number of steering angles (more than 11) for each probe would lead to more decorrelation between the images of the two probes, given the large motion and contraction of the heart, and variability in heart rate from cycle to cycle. The US data were compounded in receive mode to improve image quality and the frame rate *Fr* of the interleaved, multi-perspective, high frame rate imaging system is calculated in the following equation:

$$Fr = \frac{1}{(2N_a - 1)t_{BA} + t_{BF}} \tag{1}$$

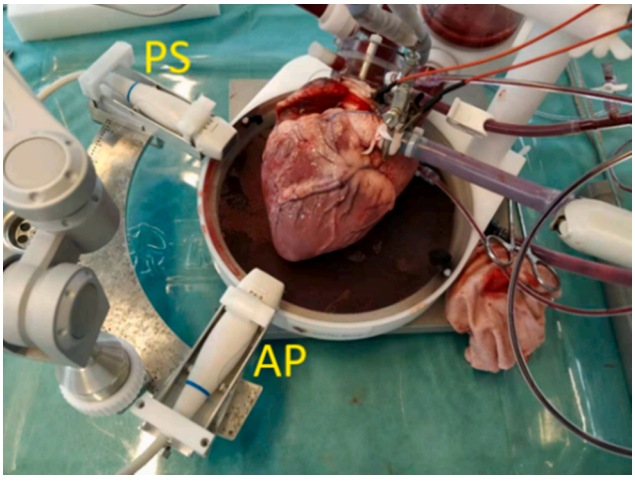

Fig. 1. Experimental PhysioHeart™ setup including the arch and two phased array probes located at the parasternal (PS) and apical (AP) positions.

where $N_a = 11$ is the number of steering angles, $t_{BA} = 260$ μs is the waiting time between different steering angles, $t_{BF} = 400$ μs is the waiting time to next acquisition and transfer acquired data to the host computer. The resulting frame rate $Fr = 170$ FPS which is more than 3 times higher than conventional cardiac US imaging.

During acquisition, all the channel data (raw US data) were sampled four times the effective center frequency of each probe. Every frame of the acquired raw US data (320 frames in total) was reconstructed and stored as in-phase quadrature (IQ) data before envelope detection for further processing in MATLAB R2019a (The MathWorks, Natick, MA, USA).

2.2. Image registration

Images obtained with the multi-perspective imaging system were registered based on a coarse-to-fine semi-automatic registration method, see Fig. 2. Because the US images from the two separate probes were acquired in an interleaved scanning sequence, temporal registration was not needed.

The coarse registration was based on matching image features (strong reflections) in the two images. The lateral wall of the epicardium at the end of diastole (ED) was used, since strong reflections around the apex and base appeared in both images. First, manual segmentation was performed by selecting a few points on the lateral wall of the epicardium. Next, the points selected on the lateral wall were interpolated and a straight line was fitted. From here, a coarse translation and rotation were obtained by matching the central points of the linear fits and calculating their slopes, respectively. Finally, the coarse registration was finished by translating and rotating the AP image sequence to the PS one.

A preliminary step before the fine registration was performed by automatically selecting the overlapping field-of-view of the two images. This removed the irrelevant image information and speeded up the computation. The fine registration was an image intensity-based iterative process [25]. The process started with specifying the transform type (rotation and translation) to generate the initial transformation matrix. Next, the metric compared the transformed moving image (AP) to the fixed image (PS) and create a metric value. Finally, the optimizer checked the stop condition based on the metric value and adjusted the transformation matrix for the next iteration. The process stopped when it approached a point of diminishing returns or the number of maximum iterations. The optimizer was based on a one-plus-one evolutionary algorithm (growth factor: 1.05, epsilon: 1.5, initial radius: 0.0063, maximum iterations: 200) and the metric was defined by measuring the mutual information of the two images, i.e., maximization of the mutual entropy in the two images [26,27]. From here, the best registration of the ED frame can be found.

The previous steps were repeated to find the best alignment for three more frames in the cardiac cycle (MS: mid of systole, ES: end of systole, MD: mid of diastole). Next, these four best alignments were registered on a whole cardiac cycle, the score of the final best alignment was decided by root mean square error (RMSE), where the lowest mean of RMSE determined the best alignment of the whole acquisition. Finally, to obtain a large field-of-view, the best registration was performed on the original envelop detected image datasets.

2.3. Image fusion

In this study, two fusion algorithms based on steerable pyramid (SP) and discrete wavelet transform (DWT) were adapted to fuse the US images (envelope data) obtained from the two probes and their performance was compared.

SP has proven to be more shift and rotation invariant in image fusion compared to other pyramidal algorithms such as Laplacian, contrast, ratio, and morphology pyramid methods [28–30]. Due to the directional selective nature of the steerable pyramid filters, it can effectively preserve contours and textures in image fusion. The decompositions of the registered images are performed resulting in a high-pass residual band and a low-pass subband L_0. Next, this low-pass band is split into a

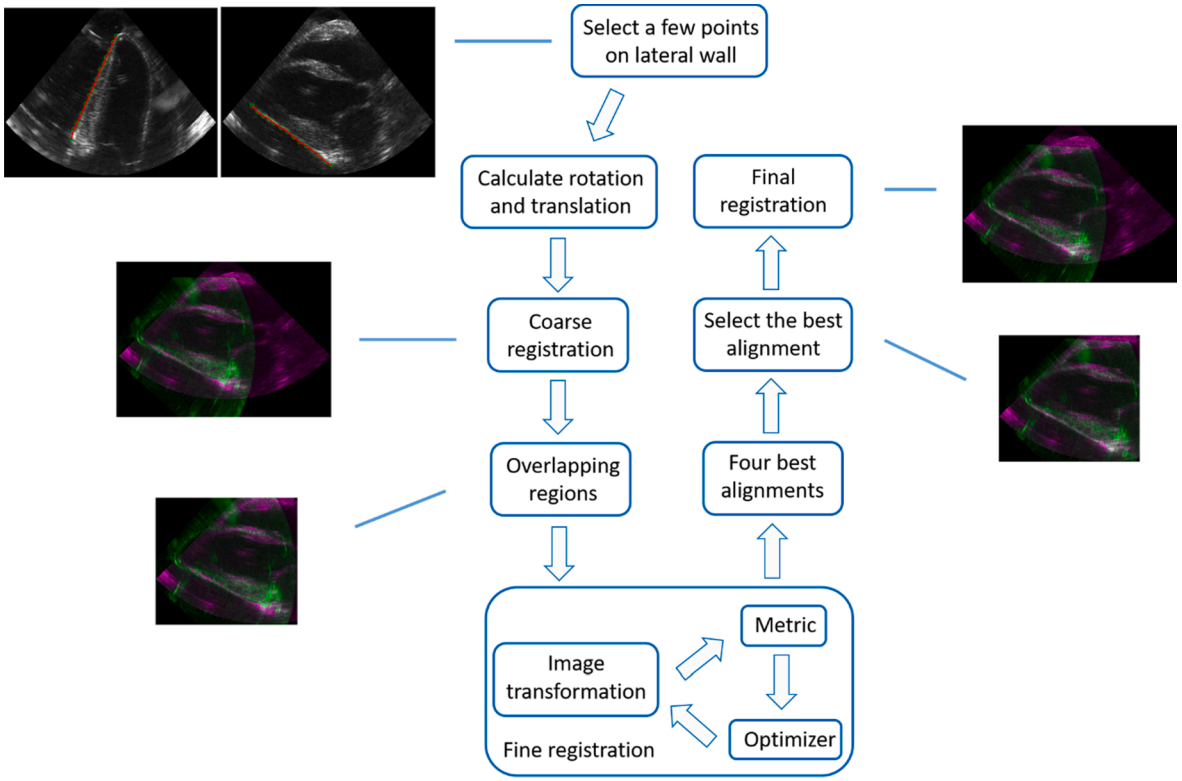

Fig. 2. Overview of the coarse-to-fine semi-automatic image registration.

another low-pass band L_1 and K + 1 oriented subbands{B_0, B_1, … , B_k}. By recursively decomposing the low-pass band L_1, the pyramid is built.

In this study, images from the two probes were decomposed into 5 levels and 4 orientation subbands individually, as Fig. 3 shows. The final low-pass subband contains the large structures of the images. The maximum values of the dual-probe images were taken, in order to preserve these larger structures of the left ventricular wall. High frequency subbands (Level 1–5) show small structures, e.g., the noise and speckles, in the US images. Hence, for these subbands, averaging was performed.

DWT preserves different frequency information in stable form and allows good localization both in time and spatial frequency domain [31,32]. The equation of DWT decomposition for 1-D is formulated as [33,34]:

$$\mathrm{DWT}(m,k) = \frac{1}{2^m}\sum_{n=0}^{N-1} s(n)g(\frac{k-n2^m}{2^m}) \tag{2}$$

where $s(n)$ is the original signal, N is the number of samples in the windowed signal, function $g(\cdot)$ is the mother wavelet, and m is the index of decomposition levels. DWT can be interpreted as a multi-stage filter bank with high-pass and low-pass filters performing a series of dilations. Subbands (coefficients) obtained after the high-pass filters are called high frequency subbands, while those resulting from the low-pass filters are called low frequency subbands. For a 2-D DWT, a 1-D DWT is first performed on the rows and then on the columns of the data. This results in three sets of high frequency subbands (horizontal, vertical, diagonal subband) and one low frequency subband. In this way, each image can be decomposed into 4 sub images: LL (low frequency subband), LH (vertical subband), HL (horizontal subband) and HH (diagonal subband) [35–37]. Subsequently, LL can be split into 4 sub images and so on. LL contains the structure of the image and the area where grey values change smoothly. LH, HL and HH show the small details of the images, such as edges of structures, speckles, and noise.

In this study, Haar wavelet was chosen as the mother wavelet to perform the decomposition of DWT [38], and the images were decomposed into 2 levels with 7 subbands (see Fig. 3). The fusion rules applied on DWT were defined as follows: for low frequency subband LL_2 which encompasses the structures of the left ventricular wall, the maximum values of the two images were taken. For high frequency subbands (LH, HL and HH), a fusion rule based on regional energy was applied to optimize the fusion of the small details in the two images [39,40], with the aim to maximally preserve the edges and speckles. The equations of the regional energy are:

$$E(x,y) = \sum_{i=-1}^{1}\sum_{j=-1}^{1} w(2+i,2+j)*Q(x+i,y+j)$$

$$Q(x,y) = I(x,y)^2$$

$$w = \frac{1}{16}\begin{bmatrix}1 & 2 & 1\\ 2 & 4 & 2\\ 1 & 2 & 1\end{bmatrix} \tag{3}$$

where w is a 3 × 3 kernel, and $I(x,y)$ is the high frequency subband of the decomposed image.

Next, the similarity of the regional energies of the two images was calculated and the threshold of the similarity was defined, using the similarity of the regional energy of the two images $S(x,y)$:

$$S(x,y) = \frac{2\sum_{i=-1}^{1}\sum_{j=-1}^{1} w(2+i,2+j)*P(x+i,y+j)}{E_1(x,y)+E_2(x,y)}$$

$$P(x,y) = I_1(x,y)*I_2(x,y) \tag{4}$$

where $E_1(x,y)$ and $E_2(x,y)$ are the regional energies of the two images respectively. The threshold of the similarity is calculated using:

$$I_{FH}(x,y) = \begin{cases} I_{1H}(x,y), & S(x,y) \le T \& E_1(x,y) > E_2(x,y)\\ I_{2H}(x,y), & S(x,y) \le T \& E_1(x,y) \le E_2(x,y)\\ W_{max}I_1(x,y) + W_{min}I_2(x,y), & S(x,y) > T \& E_1(x,y) > E_2(x,y)\\ W_{\min}I_1(x,y) + W_{\max}I_2(x,y), & S(x,y) > T \& E_1(x,y) \le E_2(x,y)\end{cases}$$

$$W_{\min} = \frac{S(x,y)-T}{2(1-T)}$$

$$W_{\max} = 1 - W_{\min}$$

$$T = 0.65 \tag{5}$$

As Eq. (5) shows, T is the threshold of the similarity, $W_{\max}$ and $W_{\min}$ are the weights of averaging. If $S(x,y) \le T$, it implies that the difference of the regional energies of the two images is large. In this case, the wavelet coefficient of the image with a larger regional energy is chosen. If $S(x,y) > T$, the regional energies of the two images are close to each other, so weighted averaging is used to fuse the images.

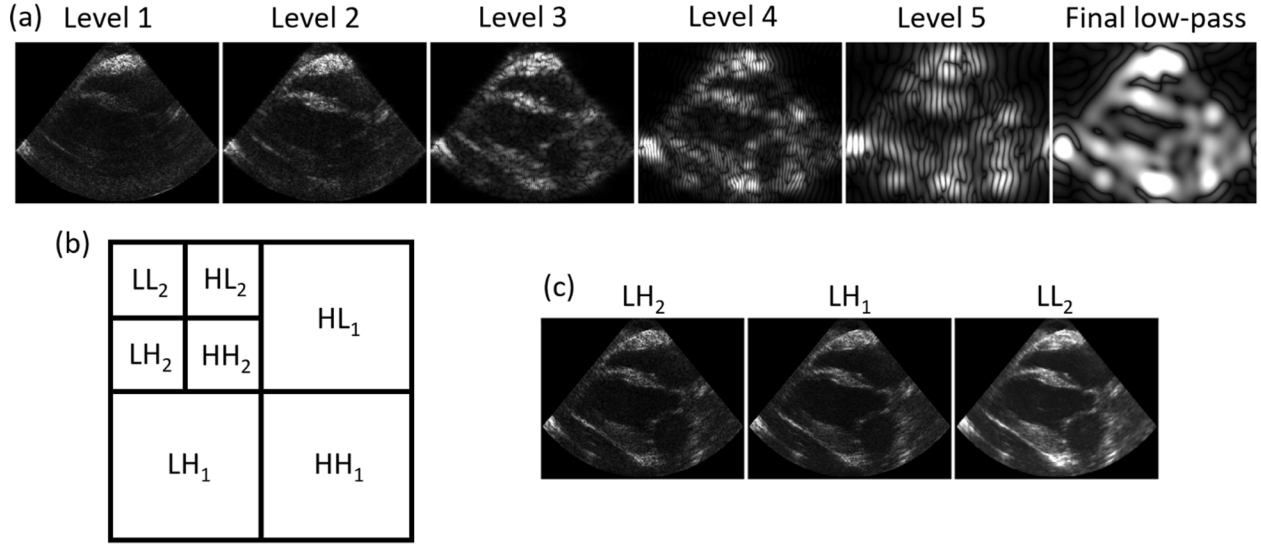

Fig. 3. Decompositions of SP and DWT. Images were decomposed into different structures, small structures on the left and large structures on the right. (a) An example of SP using 5 levels with vertical orientation subband, the top right image is the final low-pass subband. (b) DWT decomposition with 2 levels. (c) An example of the LH (vertical subband) and LL_2 (low frequency subband) using DWT decomposition with 2 levels.

2.4. Speckle statistics

First- and second-order speckle statistics were calculated to assess improvements in image quality (contrast) and spatial resolution of the interleaved multi-probe imaging system, respectively. First-order speckle statistics encompasses grey level histogram analysis, quantified by the histogram overlap percentage (OL). In addition, the contrast-to-noise ratio (CNR) between the myocardium and endocardium, as well as the mean gradient (MG) and entropy of the myocardium were calculated, all to assess contrast. Second-order speckle statistics quantify the resolution of the ultrasound image system by estimating the speckle size. The aforementioned speckle statistics analyzes were performed on all four images: AP, PS, F1 (fusion based on SP) and F2 (fusion based on DWT).

First-order speckle statistics describe the probability distribution of gray values for a given tissue and specific probe and acquisitions scheme. In this study, histogram analysis was performed to compare the probability distribution of the speckles on the left ventricular wall in single probe and fused images. As Fig. 4(a) shows, myocardium and endocardium were both manually segmented into 12 regions. To compare the distinction between myocardium and endocardium in AP, PS, F1 and F2, the OL of the gray value histograms of the myocardium and endocardium was calculated for the four images.

Next, to quantify the visibility of the left ventricular wall in all four images, the CNR was estimated according to the following equation:

$$CNR = \frac{\mu_m - \mu_e}{\sqrt{\sigma_m^2 + \sigma_e^2}} \tag{6}$$

where μ_m and μ_e are the mean pixel intensities of the myocardium and endocardium respectively, σ_m and σ_e denote their standard deviation.

In order to compare the performances of the two fusion algorithms, the mean gradient and entropy of all the segmented regions in myocardium of all four images were quantified, using the following equations:

$$\begin{aligned} G_{xy}(j) &= |G_x(j)| + |G_y(j)| \\ MG &= \frac{\sum_{j=1}^{N} G_{xy}(j)}{N} \end{aligned} \tag{7}$$

$$E = -\sum_{i=0}^{L-1} P_i \log_2 P_i \tag{8}$$

where G_x and G_y are the gradients of each pixel in X and y direction, and N is all the pixels in one region. MG is the mean gradient of each region. P is the probability of gray scale i appearing in the histogram of each region. L is the number of gray scale values in the histogram analysis. E is the entropy of every region. MG shows the change rate of the gray scale, and is commonly used as an indicator for image fusion to quantify the ability of differentiating small details in the image [41,42]. The entropy of an image is a statistical measure of the degree of randomness in the image. Hence, entropy represents the information present in the image and can be used to characterize the texture of the input image [43,44].

Second-order speckle statistics indicate spatial characteristics of the speckle pattern, which can be used to calculate the point-spread function of the system [45,46]. As Fig. 4(b) shows, a box (yellow square) was defined within each region of the segmentation, and the autocorrelation function was calculated using all data points (and thus speckles) in the box of each region. The full-width half maximum (FWHM) of the resulting normalized autocorrelation function was computed, see Fig. 4 (d). To compare the resolution of single and multi-probe images, the major and minor axis length of the resulting shape and corresponding eccentricity were calculated.

3. Results

The coarse-to-fine registration of the images was performed successfully in all three hearts. The best alignment was determined by the lowest RMSE found during a whole cardiac cycle. The rotation error of the best alignment was less than 0.7° in all hearts. Quantitative results of image registration are shown in Table 1. The whole registration process took around 5 min for one heart. Five volunteers were asked to perform the manual step (select a few points on the lateral wall of the epicardium). The difference of the final registration results after using the semi-automatic registration method is less than 0.5° for all three hearts.

A more precise alignment of the two images can be achieved after fine registration compared to coarse registration. Fused images from single perspectives show increased image clarity, more distinguishable shapes of the LV and a larger field-of-view (+28.3%), as Fig. 5 shows.

CNR values in the fused images have increased considerably in all three hearts, as Fig. 6 shows. The total CNR increased from 1.1 to 1.4, CNR in the 'axial regions' (see Fig. 4 for definition) increased from 1.1 to 1.5, and CNR in the 'lateral regions' increased from 1.0 to 1.2. During the entire cardiac cycle, the increase in CNR was maintained despite tissue motion as can be seen in Fig. 7. In addition, a reduced overlap in gray value histogram between myocardium and endocardium was found in the fused images, see Fig. 6. The total OL decreased from 0.32 to 0.21, axial OL decreased from 0.35 to 0.19, and lateral OL decreased from 0.41 to 0.26.

The performances of the two fusion algorithms for first-order speckle statistics can be depicted from Fig. 6 and Table 2. Overall, larger improvements of CNR, OL, MG and entropy were found for fusion method F2. Compared to F1, MG increased from $2.4 \cdot 10^6$ to $3.1 \cdot 10^6$ and entropy increased from 5.9 to 6.1.

Autocorrelation results are shown in Fig. 8 and Fig. 9. In the single probe images, speckles were more stretched in the lateral direction and lateral speckle size increased for larger imaging depth, e.g., from box 7 to box 12 in the AP view, as expected. Overall, major and minor axis

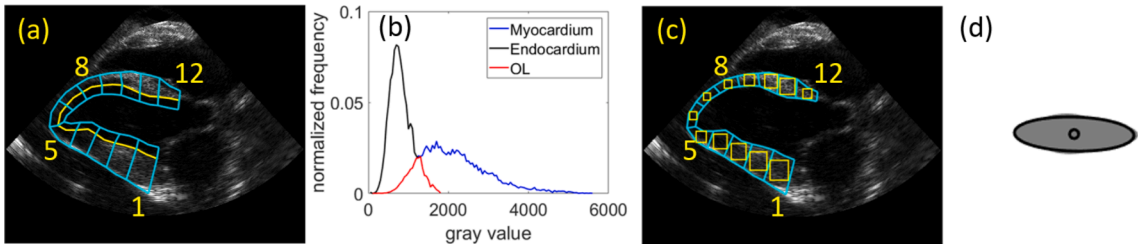

Fig. 4. Speckle statistics. (a) Endocardium and myocardium were segmented into 12 regions to analyze first-order speckle statistics. The yellow lines indicate the border between endocardium and myocardium. Axial regions: box 1–4 and 9–12, lateral regions: box 5–8. (b) An example of the first-order speckle statistics, i.e., histograms of gray values where the blue, black, and red curves represent myocardium, endocardium and overlapping regions (OL), respectively. (c) Second-order speckle statistics: a box in each region was defined to compute the autocorrelation function. (d) Half maximum of the normalized autocorrelation function indicated by the black ellipse, later used to quantify eccentricity and speckle size. The black circle is the centroid of the ellipse. (For interpretation of the references to colour in this figure legend, the reader is referred to the web version of this article.)

Table 1
Quantitative results of image registration.

Heart	1					2					3				
Frame	C	ED	MS	ES	MD	C	ED	MS	ES	MD	C	ED	MS	ES	MD
R(degree)	93.0	89.4	89.3	88.3	89.8	86.1	89.7	92.0	91.3	90.5	85.2	89.9	90.6	90.3	90.0
T_x (mm)	–33	−24	−27	−25	−24	−49	−48	−51	−50	−49	−25	–23	−25	−24	–23
T_y (mm)	19	17	15	14	17	42	48	49	49	47	17	24	25	25	24
RMSE(10^6)	2.48	2.44	2.39	2.40	2.44	5.03	5.02	5.00	5.00	4.99	3.51	3.47	3.46	3.45	3.47

* ED = End of diastole, MS = Mid of systole, ES = End of systole, MD = Mid of diastole, C = Coarse registration at ED, R = Rotation angle, T_x = Translation in x direction, T_y = Translation in y direction, RMSE = Mean of root mean square error in a whole cardiac cycle.

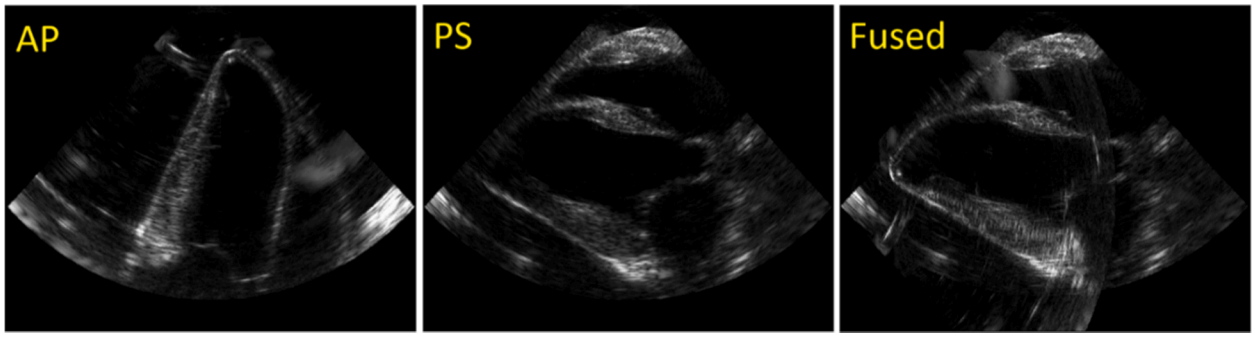

Fig. 5. Single probe and fused B-mode images. Apical view (left), parasternal long-axis view (middle), and multi-perspective view for F2 (right).

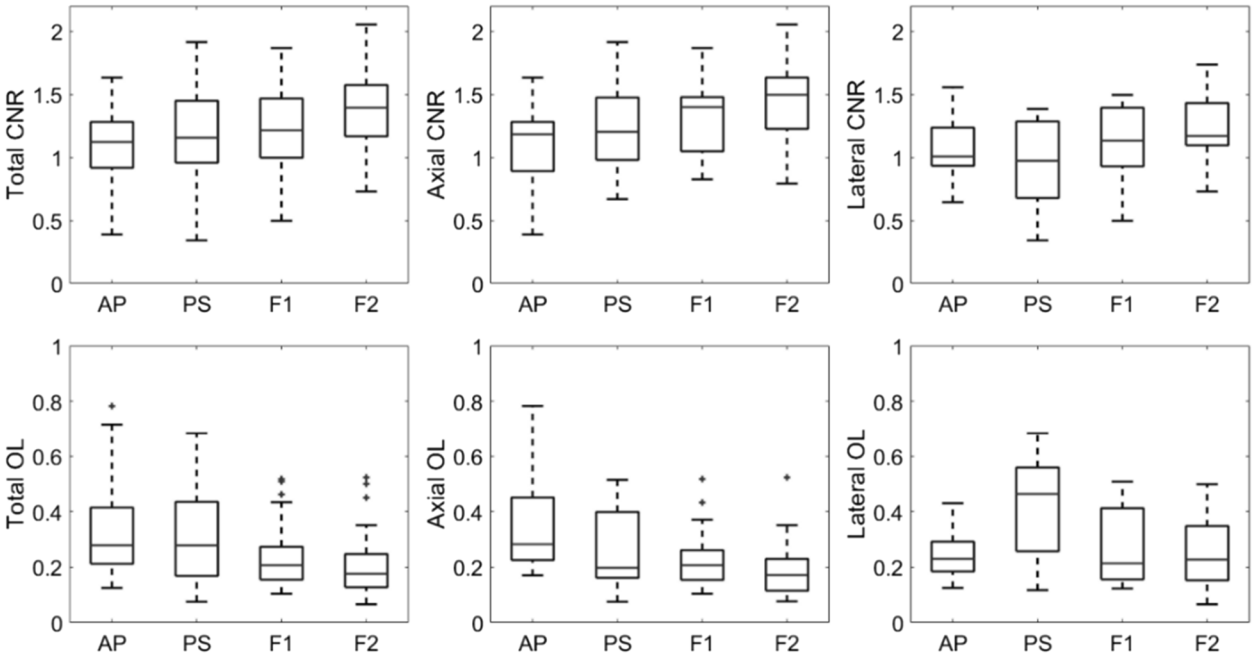

Fig. 6. Contrast-to-noise ratio (CNR) and histogram overlap (OL) for single probes images obtained in the apical (AP) and parasternal long-axis view (PS), and the fused images using fusion methods F1 and F2. Both CNR and OL are calculated for the total endocardium-myocardium interface as well as the axial and lateral sections separately.

length as well as the eccentricity of the determined point-spread functions have decreased significantly in the fused images. The average eccentricity decreased from 0.91 to 0.73, the major axis length decreased from 0.59 mm to 0.35 mm, and the minor axis length decreased slightly from 0.21 mm to 0.18 mm. Compared to F1, a larger decrease of speckle sizes can be observed despite the eccentricity is slightly higher for F2.

4. Discussion

The purpose of this study is to explore the feasibility and advantages of using two phased array probes to perform high frame rate, interleaved multi-perspective echocardiography. More specifically, we investigated the image enhancement in terms of field-of-view, image contrast, and resolution in an *ex-vivo* beating porcine heart setup. An iterative multi-scale semi-automatic registration algorithm was developed to precisely find the best alignment of the images acquired from the two probes. Two fusion algorithms were adapted to compound the image data obtained from the two probes, and their performance was compared. First- and second-order speckle statistics were computed to quantify the image quality of single probe and fused images using two fusion algorithms.

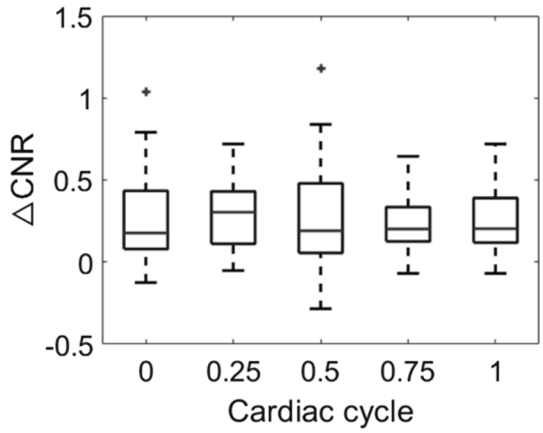

Fig. 7. Increase in contrast-to-noise ratio (CNR) from single perspective to multi-perspective ultrasound images during an entire cardiac cycle.

For the image acquisition, one of the biggest challenges was to ensure that both probes were imaging the same plane. A mini-arch was used to ensure that the two US probes were exactly imaging the same plane, necessary to avoid misalignment in the elevational plane which would render fusion of the 2-D imaging data impossible. Moreover, the arch served a double purpose since it provided the ground truth of the rotation angle (90°) of the two probes to verify the registration.

The coarse-to-fine semi-automatic registration algorithm was performed successfully with a rotation error less than 0.7° in all hearts. The only manual step in this algorithm was to select a few points on the lateral wall of epicardium, which could be optimized in future studies. More importantly, this method automatically determined the best registration result by calculating the RMSE of the two images in a whole cardiac cycle without using the ground truth. However, due to the lack of ground truth data in translation, the error in estimates of the translation error cannot be evaluated quantitatively. The intensity based iterative fine registration is suitable for finding the precise alignment, when provided with a good initial guess. However, because of the large rotation, anisotropic resolution and contrast of the two images in this application, it remains challenging to perform it fully automatically with a high accuracy.

Two image fusion algorithms were adapted to combine the registered two images. The main advantage of the SP method is that the representation is shift invariant, which means no aliasing in subbands. This strength makes it suitable to decompose image features into different structures. The primary disadvantage is the low computational efficiency, since the representation of SP is substantially overcomplete [47]. DWT produces a non-redundant image representation and is relatively computationally efficient. The main drawback of DWT is the fact that the representation is shift variant, which may result in aliasing or spatial ringing in the images [48,49]. However, the aliasing mainly occurs when the levels chosen for DWT decomposition were high, and also depends on the types of images, and mother wavelets chosen. With the image sets acquired in this study, we have discovered that using the Haar wavelet to decompose images into less than 3 levels can avoid the

Table 2
Quantitative results: mean gradient (MG) and entropy.

Heart	1				2				3			
Probe	AP	PS	F1	F2	AP	PS	F1	F2	AP	PS	F1	F2
MG (10^6)	1.53	1.65	1.89	2.50	2.23	2.68	2.91	3.85	1.65	2.22	2.32	3.07
Entropy	4.26	4.06	5.11	5.42	5.09	5.68	6.56	6.73	5.59	5.98	6.14	6.25

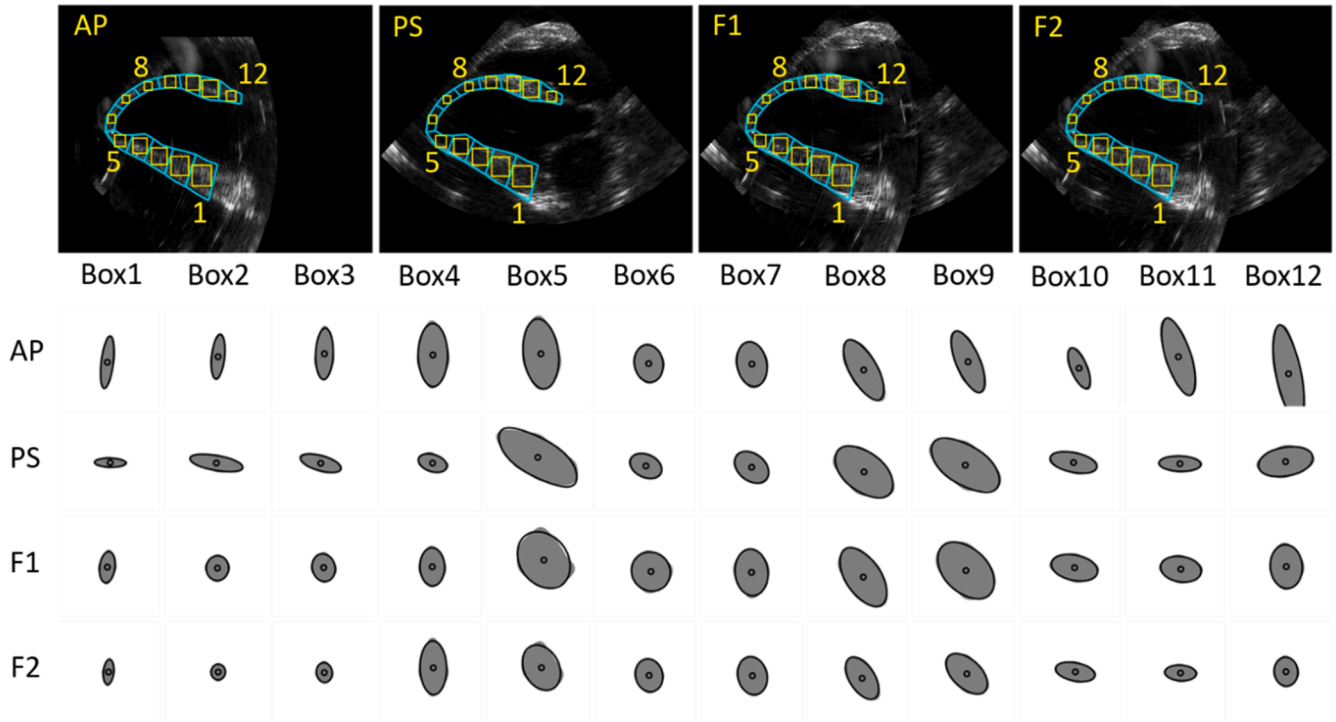

Fig. 8. Second-order speckle results for single probe images obtained in the parasternal (PS) and apical view (AP), as well for fused images using the two fusion methods (F1 and F2).

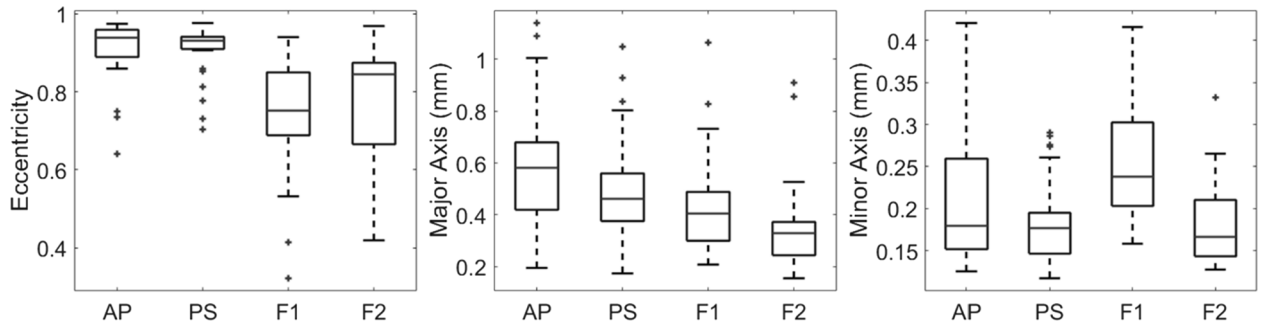

Fig. 9. Eccentricity (left), major axis length (middle) and minor axis length (right) resulting from the second-order speckle analysis on images obtained with single probe apical (AP) and parasternal images (PS) and the fused images (F1 and F2).

aliasing issues in reconstructed images. Therefore, we chose 2 decomposition levels for DWT fusion. On one hand, it can speed up the computation time for image decomposition and reconstruction. One the other hand, the 7 subbands (1 low frequency, 6 high frequency) were able to differentiate the different structures in the US images for fusion.

First-speckle statistics results have shown that the image quality, specifically the CNR and distinction between endocardium and myocardium, has improved significantly after fusion, as Fig. 6 shows. It can be seen that PS had a higher axial CNR and less histogram OL than AP while AP had a higher lateral CNR and less histogram OL than PS. This is because, for the axial regions, more backscatter is generated in the PS view, while for the lateral regions more ultrasound reflections are detected in the AP view. One can appreciate that a higher image contrast and clearer interface between endocardium and myocardium were achieved in both axial and lateral regions after fusion, during the whole cardiac cycle.

The mean gradient in F2 always showed the highest values, indicating a substantial improvement in presence of differentiating speckle patterns, while F1 did not always have a higher MG over single probes (Table 2). This can be explained by the different fusion rules applied to the high frequency subbands for F1 and F2. In the high frequency subbands, more speckles and important image features, e.g. edges, are found. Hence, averaging does not seem to be the optimal approach to compound the two images. The regional energy based fusion rule successfully extracted the edges and small features in the two images. In addition, the results of entropy on the left ventricular wall also demonstrated that more information (e.g., speckles) in the myocardium can be derived from the images when using F2. One can argue that the increase in entropy after fusion may come from noise. However, since the CNR was also higher after fusion, the increased entropy is most likely the result of an increased level of structure and speckle.

Second-order speckle statistics results clearly indicate that the resolution after fusion has been vastly enhanced. However, in some regions, e.g. box 4 and 6 in PS, there were not enough speckles present. The fusion in these regions mostly used image data from the AP view. Hence, resulting speckles after fusion had similar eccentricities and sizes as found in the AP view. Moreover, in some regions mainly strong reflections were present with little speckles, e.g., box 5, 8 and 9. As a result, oversized speckles were determined in the PS view. However, by taking the speckles from AP into account, the speckle sizes in these regions decreased vastly after fusion, leading to an improved resolution.

For the results of speckle size, one can appreciate that speckle sizes were greatly reduced in F2 compared to single probes and F1, resulting in a significant improvement of the lateral resolution. Compared to F1, a stronger reduction of speckle sizes can be observed despite the slightly higher eccentricity in F2. In some cases, speckle sizes were even enlarged in F1, e.g. box 5–10. There are two possible explanations. First of all, speckles were averaged from the two probes in F1, while speckles were fused based on a regional energy based fusion rule in F2. This means that speckles were only weight averaged when the difference of the regional energy of the two images was close to the threshold we chose. When the difference was bigger than the threshold, only the speckles in the image that contain higher regional energy will be selected for fusion. Secondly, the mother wavelet and decomposition levels chosen to decompose the images also played an essential role.

For each probe, the limitations in aperture and steering angle, due to the presence of ribs, are similar to those for conventional single probe imaging [10]. The use of two probes is introduced to overcome these limitations. Of course clutter will remain present in the individual images when ribs are present, but the benefits of simulating 'large steering angles' by adding a second probe are clear.

The two probes were positioned at apical and parasternal views in 90° to show the ultimate benefits in terms of image quality. *In vivo*, when ribs and surrounding structures are present, it will take some time for the sonographer to find the ideal imaging position and corresponding view for each of the two probes. In some cases, when only a smaller relative angle between the two probes is achievable, multi-perspective US will still improve image quality.

There are some limitations of this study. First of all, the system operates in 2-D mode which does not capture the full geometry and motion of the heart. Here, 3-D US imaging is the obvious next step but at the cost of a lower frame rate, decreased image quality, and increased system complexity. Secondly, the *ex-vivo* setup allows the use of a mini-arch to avoid misalignment of the two probes. The mini-arch was not designed for *in vivo* or clinical usage. This will require more flexible probe fixation or probe tracking devices [50,51]. In fact, a probe fixation device (hand-free) for *in vivo* measurements has already been developed and demonstrated for one probe [51]. It can be easily altered into a dual-probe fixation device with all the necessary degrees of freedom to ensure a common imaging plane. Ultimately, the use of 3-D ultrasound, as well as the introduction and emergence of patch-based devices will change clinical ultrasound, enabling and catalyzing multi-perspective US imaging even further. Accordingly, we are positive that the multi-perspective US imaging method proposed can be adapted and modified for *in vivo* application. Nevertheless, this is beyond the scope of this study so far. Thirdly, although the *ex-vivo* beating porcine hearts have a high level of realism compared to simulations and phantoms, there is no surrounding tissue present, such as ribs and lungs, which will probably lead to attenuation of the US and introduce clutter artifacts. This may bring new challenges for the registration. To cope with this, clutter reduction algorithms such as, wavelet and singular value decomposition (SVD) filter can be adapted to filter out the clutter artifacts and preserve the anatomical structures [52,53].

5. Conclusion

In this study, multi-perspective high frame rate ultrasound imaging of the heart using two phased array probes was demonstrated in an *ex-vivo* beating porcine heart setup. Advantages in image quality of this method have been demonstrated, showing enlarged field-of-view, and

enhanced image contrast and resolution. Future work will focus on validating this technique to improve functional measurements, e.g., cardiac strain imaging, in 2-D and 3-D, and extending this method for right ventricular imaging.

Declaration of Competing Interest

The authors declare the following financial interests/personal relationships which may be considered as potential competing interests: Richard Lopata reports financial support was provided by European Research Council.

Acknowledgements

This work is part of the MUSE project, which has received funding from the European Research Council (ERC) under the European Union's Horizon 2020 research and innovation programme (ERC starting grant 757958). The efforts in building the mini-arch for the *ex-vivo* beating porcine hearts experiments by Jurgen Bulsink, employed by Eindhoven University of Technology (Eindhoven, Netherlands) are kindly acknowledged.

References

[1] J.A. Jensen, Medical ultrasound imaging, Prog. Biophys. Mol. Biol. 93 (1) (Jan. 2007) 153–165, https://doi.org/10.1016/j.pbiomolbio.2006.07.025.
[2] T. Rahman, M. S. Uddin, Speckle noise reduction and segmentation of kidney regions from ultrasound image, in: 2013 International Conference on Informatics, Electronics and Vision (ICIEV), May 2013, pp. 1–5. http://doi.org/10.1109/ICIEV.2013.6572601.
[3] T. Ma, M. Yu, Z. Chen, C. Fei, K.K. Shung, Q. Zhou, Multi-frequency intravascular ultrasound (IVUS) imaging, IEEE Trans. Ultrason. Ferroelectr. Freq. Control 62 (1) (Jan. 2015) 97–107, https://doi.org/10.1109/TUFFC.2014.006679.
[4] T. Ding, S. Zhang, Q. Fu, Z. Xu, M. Wan, Ultrasound line-by-line scanning method of spatial–temporal active cavitation mapping for high-intensity focused ultrasound, Ultrasonics 54 (1) (Jan. 2014) 147–155, https://doi.org/10.1016/j.ultras.2013.04.011.
[5] H.-L. Liu, S.-M. Huang, M.-L. Li, High frame rate ultrasound monitoring of high intensity focused ultrasound-induced temperature changes: A novel asynchronous approach, Med. Phys. 37 (11) (2010) 5921–5928, https://doi.org/10.1118/1.348890210.1118/1.3488902.1.
[6] G. Montaldo, M. Tanter, J. Bercoff, N. Benech, M. Fink, Coherent plane-wave compounding for very high frame rate ultrasonography and transient elastography, IEEE Trans. Ultrason. Ferroelectr. Freq. Control 56 (3) (Mar. 2009) 489–506, https://doi.org/10.1109/TUFFC.2009.1067.
[7] C. Papadacci, M. Pernot, M. Couade, M. Fink, M. Tanter, High-contrast ultrafast imaging of the heart, IEEE Trans. Ultrason. Ferroelectr. Freq. Control 61 (2) (Feb. 2014) 288–301, https://doi.org/10.1109/TUFFC.2014.6722614.
[8] H. Hasegawa, C.L. De Korte, Special Issue on Ultrafast Ultrasound Imaging and Its Applications, Appl. Sci., vol. 8, no. 7, Art. no. 7, Jul. 2018, http://doi.org/10.3390/app8071110.
[9] H.H.G. Hansen, R.G.P. Lopata, C.L. de Korte, Noninvasive Carotid Strain Imaging Using Angular Compounding at Large Beam Steered Angles: Validation in Vessel Phantoms, IEEE Trans. Med. Imaging 28 (6) (Jun. 2009) 872–880, https://doi.org/10.1109/TMI.2008.2011510.
[10] H.H.G. Hansen, R.G.P. Lopata, T. Idzenga, C.L. de Korte, Full 2D displacement vector and strain tensor estimation for superficial tissue using beam-steered ultrasound imaging, Phys. Med. Biol. 55 (11) (May 2010) 3201–3218, https://doi.org/10.1088/0031-9155/55/11/014.
[11] W.-N. Lee, Z. Qian, C.L. Tosti, T.R. Brown, D.N. Metaxas, E.E. Konofagou, Preliminary Validation of Angle-Independent Myocardial Elastography Using MR Tagging in a Clinical Setting, Ultrasound Med. Biol. 34 (12) (Dec. 2008) 1980–1997, https://doi.org/10.1016/j.ultrasmedbio.2008.05.007.
[12] A. Nasis, P.M. Mottram, J.D. Cameron, S.K. Seneviratne, Current and Evolving Clinical Applications of Multidetector Cardiac CT in Assessment of Structural Heart Disease, Radiology 267 (1) (Apr. 2013) 11–25, https://doi.org/10.1148/radiol.13111196.
[13] H.L. Fred, Drawbacks and Limitations of Computed Tomography, Tex Heart Inst J 31 (4) (2004) 345–348.
[14] P. Hoskins, S. Semple, P. White, J. Richards, Imaging of Aneurysms, in: Biomechanics and Mechanobiology of Aneurysms, T. McGloughlin, Ed. Berlin, Heidelberg: Springer, 2011, pp. 35–65. http://doi.org/10.1007/8415_2010_64.
[15] K. Rajpoot, V. Grau, J.A. Noble, C. Szmigielski, H. Becher, Multiview Fusion 3-d Echocardiography: Improving the Information and Quality of Real-Time 3-D Echocardiography, Ultrasound Med. Biol. 37 (7) (Jul. 2011) 1056–1072, https://doi.org/10.1016/j.ultrasmedbio.2011.04.018.
[16] C. Yao, J.M. Simpson, T. Schaeffter, G.P. Penney, Multi-view 3D echocardiography compounding based on feature consistency, Phys. Med. Biol. 56 (18) (Aug. 2011) 6109–6128, https://doi.org/10.1088/0031-9155/56/18/020.
[17] D. Augustine, M. Yaqub, C. Szmigielski, E. Lima, S.E. Petersen, H. Becher, J. A. Noble, P. Leeson, '3D Fusion' Echocardiography Improves 3D Left Ventricular Assessment: Comparison with 2D Contrast Echocardiography, Echocardiography 32 (2) (2015) 302–309, https://doi.org/10.1111/echo.12655.
[18] C. Szmigielski, K. Rajpoot, V. Grau, S.G. Myerson, C. Holloway, J.A. Noble, R. Kerber, H. Becher, Real-Time 3D Fusion Echocardiography, JACC: Cardiovascular Imaging 3 (7) (2010) 682–690.
[19] A. Haak, B. Ren, H.W. Mulder, G. Vegas-Sánchez-Ferrero, G. van Burken, A.F. W. van der Steen, M. van Stralen, J.P.W. Pluim, T. van Walsum, J.G. Bosch, Improved Segmentation of Multiple Cavities of the Heart in Wide-View 3-D Transesophageal Echocardiograms, Ultrasound Med. Biol. 41 (7) (2015) 1991–2000, https://doi.org/10.1016/j.ultrasmedbio.2015.03.011.
[20] H.W. Mulder, M. van Stralen, H.B. van der Zwaan, K.Y.E. Leung, J.G. Bosch, J.P. W. Pluim, Multiframe registration of real-time three-dimensional echocardiography time series, J. Med. Imag 1 (1) (2014) 014004, https://doi.org/10.1117/1.JMI.1.1.014004.
[21] L. Peralta, A. Gomez, Y. Luan, B.-H. Kim, J.V. Hajnal, R.J. Eckersley, Coherent Multi-Transducer Ultrasound Imaging, IEEE Trans. Ultrason. Ferroelectr. Freq. Control 66 (8) (2019) 1316–1330, https://doi.org/10.1109/TUFFC.2019.2921103.
[22] L. Peralta, A. Gomez, J.V. Hajnal, R.J. Eckersley, Coherent multi-transducer ultrasound imaging in the presence of aberration, in: Medical Imaging 2019: Ultrasonic Imaging and Tomography, Mar. 2019, vol. 10955, p. 109550O. http://doi.org/10.1117/12.2511776.
[23] H. de Hoop, N.J. Petterson, F.N. van de Vosse, M.R.H.M. van Sambeek, H.-M. Schwab, R.G.P. Lopata, Multiperspective Ultrasound Strain Imaging of the Abdominal Aorta, IEEE Trans. Med. Imaging 39 (11) (Nov. 2020) 3714–3724, https://doi.org/10.1109/TMI.2020.3003430.
[24] J. de Hart, A. de Weger, S. van Tuijl, J.M.A. Stijnen, C.N. van den Broek, M.C. M. Rutten, B.A. de Mol, An Ex Vivo Platform to Simulate Cardiac Physiology: A New Dimension for Therapy Development and Assessment, Int J Artif Organs 34 (6) (2011) 495–505, https://doi.org/10.5301/IJAO.2011.8456.
[25] M. Lee, S. Kim, I. Seo, Intensity-based registration of medical images, in: 2009 International Conference on Test and Measurement, Dec. 2009, vol. 1, pp. 239–242. http://doi.org/10.1109/ICTM.2009.5412952.
[26] M. Styner, C. Brechbuhler, G. Szckely, G. Gerig, Parametric estimate of intensity inhomogeneities applied to MRI, IEEE Trans. Med. Imaging 19 (3) (Mar. 2000) 153–165, https://doi.org/10.1109/42.845174.
[27] S. Raghunathan, D. Stredney, P. Schmalbrock, B. D. Clymer, Image Registration Using Rigid Registration and Maximization of Mutual Information, p. 1.
[28] Z. Liu, K. Tsukada, K. Hanasaki, Y.K. Ho, Y.P. Dai, Image fusion by using steerable pyramid, Pattern Recogn. Lett. 22 (9) (Jul. 2001) 929–939, https://doi.org/10.1016/S0167-8655(01)00047-2.
[29] J. Portilla, E.P. Simoncelli, A Parametric Texture Model Based on Joint Statistics of Complex Wavelet Coefficients, Int. J. Comput. Vision 40 (1) (Oct. 2000) 49–70, https://doi.org/10.1023/A:1026553619983.
[30] J. Du, W. Li, B. Xiao, Q. Nawaz, Union Laplacian pyramid with multiple features for medical image fusion, Neurocomputing 194 (Jun. 2016) 326–339, https://doi.org/10.1016/j.neucom.2016.02.047.
[31] P. Geng, X. Sun, J. Liu, Adopting Quaternion Wavelet Transform to Fuse Multi-Modal Medical Images, J. Med. Biol. Eng. 37 (2) (Apr. 2017) 230–239, https://doi.org/10.1007/s40846-016-0200-6.
[32] R. Singh, M. Vatsa, A. Noore, Multimodal Medical Image Fusion Using Redundant Discrete Wavelet Transform, in: 2009 Seventh International Conference on Advances in Pattern Recognition, Feb. 2009, pp. 232–235. http://doi.org/10.1109/ICAPR.2009.97.
[33] D.C. Robertson, O.I. Camps, J.S. Mayer, W.B. Gish, Wavelets and electromagnetic power system transients, IEEE Trans. Power Delivery 11 (2) (Apr. 1996) 1050–1058, https://doi.org/10.1109/61.489367.
[34] L. Lei, C. Wang, X. Liu, Discrete Wavelet Transform Decomposition Level Determination Exploiting Sparseness Measurement, Int. J. Electr. Comput. Eng. 7 (9) (Sep. 2013) 1182–1185.
[35] M.A. Berbar, S.F. Gaber, N.A. Ismail, Image fusion using multi-decomposition levels of discrete wavelet transform, pp. 294–297, Jan. 2003, http://doi.org/10.1049/cp:20030545.
[36] Y. Yang, A Novel DWT Based Multi-focus Image Fusion Method, Procedia Eng. 24 (Jan. 2011) 177–181, https://doi.org/10.1016/j.proeng.2011.11.2622.
[37] A. Anoop Suraj, M. Francis, T.S. Kavya, T.M. Nirmal, Discrete wavelet transform based image fusion and de-noising in FPGA, J. Electr. Syst. Inf. Technol. 1 (1) (2014) 72–81.
[38] R.S. Stanković, B.J. Falkowski, The Haar wavelet transform: its status and achievements, Comput. Electr. Eng. 29 (1) (Jan. 2003) 25–44, https://doi.org/10.1016/S0045-7906(01)00011-8.
[39] X. Liu, Y. Zhou, J. Wang, Image fusion based on shearlet transform and regional features, AEU – Int. J. Electron. Commun. 68 (6) (Jun. 2014) 471–477, https://doi.org/10.1016/j.aeue.2013.12.003.
[40] X. Su-xia, C. Tian-hua, L. Jing-xian, Image fusion based on regional energy and standard deviation, in: 2010 2nd International Conference on Signal Processing Systems, Jul. 2010, vol. 1, pp. V1-739–V1-743. http://doi.org/10.1109/ICSPS.2010.5555262.
[41] R. Ryan, B. Baldridge, R.A. Schowengerdt, T. Choi, D.L. Helder, S. Blonski, IKONOS spatial resolution and image interpretability characterization, Remote Sens. Environ. 88 (1) (Nov. 2003) 37–52, https://doi.org/10.1016/j.rse.2003.07.006.
[42] B. Huang, F. Yang, M. Yin, X. Mo, C. Zhong, A Review of Multimodal Medical Image Fusion Techniques, Comput. Math. Methods Med. 2020 (2020) 1–16, https://doi.org/10.1155/2020/8279342.

[43] D.-Y. Tsai, Y. Lee, E. Matsuyama, Information Entropy Measure for Evaluation of Image Quality, J Digit Imaging 21 (3) (Sep. 2008) 338–347, https://doi.org/10.1007/s10278-007-9044-5.
[44] D. Wei, G. Kang, C. Hu, B. Hou, N. Zhang, Y. Tang, A New Fusion Framework for Multimodal Medical Image Based on GRWT, in: ICASSP 2019–2019 IEEE International Conference on Acoustics, Speech and Signal Processing (ICASSP), May, 2019, pp. 1194–1198, https://doi.org/10.1109/ICASSP.2019.8682444.
[45] J. Ohtsubo, The second-order statistics of speckle patterns, J. Opt. 12 (2) (Mar. 1981) 129–142, https://doi.org/10.1088/0150-536X/12/2/005.
[46] N. Meitav, E.N. Ribak, S. Shoham, Point spread function estimation from projected speckle illumination, Light: Sci. Appl., vol. 5, no. 3, Art. no. 3, Mar. 2016, http://doi.org/10.1038/lsa.2016.48.
[47] B. Beferull-Lozano, Hua Xie, A. Ortega, Rotation-invariant features based on steerable transforms with an application to distributed image classification, in: Proceedings 2003 International Conference on Image Processing (Cat. No.03CH37429), Sep. 2003, vol. 3, p. III–521. http://doi.org/10.1109/ICIP.2003.1247296.
[48] C. Sun, H. Talbot, S. Ourselin, T. Adriaansen, Digital Image Computing: Techniques and Applications: Proceedings of the VIIth Biennial Australian Pattern Recognition Society Conference, DICTA 2003. Csiro Publishing, 2003.
[49] N. Kingsbury, Complex Wavelets for Shift Invariant Analysis and Filtering of Signals, Appl. Comput. Harmon. Anal. 10 (3) (May 2001) 234–253, https://doi.org/10.1006/acha.2000.0343.
[50] C.A. Giller, A.M. Giller, A New Method for Fixation of Probes for Transcranial Doppler Ultrasound, J. Neuroimaging 7 (2) (1997) 103–105, https://doi.org/10.1111/jon199772103.
[51] O.A.E. Salden, W.M. van Everdingen, R. Spee, P.A. Doevendans, M.J. Cramer, How I do it: feasibility of a new ultrasound probe fixator to facilitate high quality stress echocardiography, Cardiovascular Ultrasound 16 (1) (Mar. 2018) 6, https://doi.org/10.1186/s12947-018-0124-0.
[52] M. Sjoerdsma, S. Bouwmeester, P. Houthuizen, F.N. van de Vosse, R.G.P. Lopata, A Spatial Near-Field Clutter Reduction Filter Preserving Tissue Speckle in Echocardiography, IEEE Trans. Ultrason. Ferroelectr. Freq. Control 68 (4) (Apr. 2021) 979–992, https://doi.org/10.1109/TUFFC.2020.3028155.
[53] R. van Hees, J.-W. Muller, F. van de Vosse, M. Rutten, M. van Sambeek, M. Wu, R. Lopata, SVD-based filtering to detect intraplaque hemorrhage using single wavelength photoacoustic imaging, JBO 26 (11) (Nov. 2021), https://doi.org/10.1117/1.JBO.26.11.116003.